A novel bio-inspired hydrogel-based lattice structure to mechanically mimic human annulus fibrosus: A finite element study

Karim Kandil, Sid Ali Kaoua, Amar Mesbah, Yuri Voznyak, Fahmi Zaïri, Fahed Zaïri

Version of Record: https://www.sciencedirect.com/science/article/pii/S002074032100504X
Manuscript_bc4d80e3c16a1c48e4be35f9aea2cd20

A novel bio-inspired hydrogel-based lattice structure to mechanically mimic human disc annulus: A finite element study

Karim Kandil[a,b], Sid Ali Kaoua[c], Amar Mesbah[d], Yuri Voznyak[e], Fahmi Zaïri[b*], Fahed Zaïri[f]

[a]ICAM Site de Lille, 6 rue Auber, 59016 Lille, France
[b]Lille University, Civil Engineering and geo-Environmental Laboratory (ULR 4515 LGCgE), 59000 Lille, France
[c]Laboratoire des Sciences et Génie des Matériaux, FGMGP, USTHB, BP32 El-Alia Bab-Ezzouar, 16111 Alger, Algeria
[d]Laboratoire de Mécanique Avancée, USTHB, BP32 El-Alia Bab-Ezzouar, 16111 Alger, Algeria
[e]Centre of Molecular and Macromolecular Studies, Polish Academy of Sciences, 90363 Lodz, Poland
[f]Ramsay Générale de Santé, Hôpital privé Le Bois, 59000 Lille, France

[*]Corresponding author. fahmi.zairi@polytech-lille.fr

Abstract

Intervertebral disc hernia and dysfunctions are the most common health problems that affect humans. For this reason, the need of disc prosthetics, and especially annulus fibrosus replacements, is becoming increasingly mandatory and urgent. In the present paper, we present a novel bio-inspired hydrogel-based replacement system with rational mechanically mimetic designs of human annulus fibrosus. The new system consists of hydrogel-based lattice structure with octagonal cells separated by polylactide fibers reinforced hydrogel-based sheets. The mechanics of the new designs may be rationally controlled by tailoring microstructure, in terms of polylactide fibers orientation and hydrogel intrinsic viscosity, and mesostructure in terms of cell walls/sheets thickness. The new designs are successfully compared to the natural annulus fibrosus mechanics in terms of nonlinear stiffness and transversal behavior while considering regional dependency. The impressive biomimetic capabilities of the proposed hydrogel-based lattice structure allow to foresee the possibility of designing personalized disc prosthesis by advanced 3D printing technologies.

Keywords: Artificial annulus fibrosus; Lattice structure; Hydrogel; Transversal behavior; Regional dependence.

1. Introduction

Intervertebral disc hernia and dysfunctions are the most common health problems that affect both young and old human bodies. Although the intervertebral disc replacements design and prosthetics production have known a remarkable evolution over recent years [1-5], discectomy and spinal fusional surgeries remain the most commonly preferred and used by surgeons [6-9]**.** Many generations of replacements have been developed. Firstly, metal or metal and polymers articulating ball and socket prosthetics appeared trying to ensure relative movements between the vertebrae regardless the real local stress-strain and local strain response of the prosthetic. They are often constrained with about three degrees of freedom and gave similar clinical outcomes of fusion surgeries without any significant progression. After, many prosthetics appeared trying to add time-dependent energy storing properties by using viscoelastic core separating two parallel highly stiff endplates that connect the adjacent vertebrae [5]. The last could guarantee six degrees of freedom to the prosthetic, mimic the damping features of the natural disc and enhance a global strain of the prosthetic under the different physiological movements. The new replacement generations use different concepts regarding the fixation method with the adjacent vertebrae as well as the core design and material. Although fixation method between prosthetic/vertebrae and the core/endplates inside the prosthetic is a main point that differentiate the existing disc implants, the core design and material remain the most important points characterizing their response and allowing them to reproduce the same behavior of the natural disc. Many concepts such in case of the CP ESP prosthetic tried to reproduce the correct disc response by designing an optimized core able to replicate the kinematics of the real disc [10]. Other prosthetics construct a core inspired from the natural disc structure such as M6-C [11-12]. Similar to the real disc, M6-C core is composed of two distinct main parts in the heart of the prosthetic core we can find a compressible polycarbonate urethane polymer replacing the nucleus that is surrounded by

ultra-high molecular-weight-polyethylene woven fibers replacing the disc annulus. This type of natural disc structure-based prosthetics demonstrates very promising clinical results [12-13]. However, the disc annulus fibrosus remains more complex, with more delicate features that are not considered in replacement modeling and manufacturing until now and that could affect the spinal mobility, recovery and long-term durability after surgery.

The intervertebral disc annulus is known to be highly heterogeneous with regional dependent microstructure/properties relationships [14-18]. The annulus mechanics changes between the different radial and circumferential regions of the same disc due to the different local quantities of the constituent elements (collagen fibers, proteoglycans, water) and the collagen organization along with interactions with the surrounding physiological medium [14-15, 18]. Especially, the transversal strains have been proved recently to show unusual behavior with negative Poisson's ratios in the disc radial direction and Poisson's ratios superior to 0.5 in the disc axial direction under a circumferential loading of the annulus fibrosus [19-22]. Those unusual transversal strains increase the damping characteristic of the disc under sudden and rough loads and their consideration in a replacement device could highly enhance its performance and efficiency. Many replacement systems have been proposed in the literature trying to replicate the annulus fibrosus response materials and geometries inspired from the real annulus micro and macro structures [23-26]. In the most recent research contributions highlighted from the literature we can see that Frost and Foster [25] were inspired from the lamellar structure and the composite composition of the annulus fibrosus to construct an annulus fibrosus scaffold from polyurethane reinforced with cellulose nanocrystals fabricated into ribbons and radially layered structure. In Nerurkar et al. [23] nanofibrous biologic laminates were suggested to replicate the form and function of the annulus fibrosus. More recently, in Ref [26] a cross-aligned 3D printable structure was designed to mimic the oriented fibers and the angle-ply architecture of the annulus fibrosus. However, all these

contributions tried to replicate mechanically the rigidity and the stress-strain response of the annulus fibrous but neglected the effect of the transversal strains and the unusual Poisson's ratios of the soft tissue which will highly affect the reproduced mechanical behavior. In this study, a novel bio-inspired hydrogel-based substitute is designed in order to mimic the accurate local mechanical response of the disc. The new substitute should be able not only to allow reproducing the complete disc stiffness but permit also controlling and varying locally this response in the different regions of the annulus and replicating accurately the unusual transversal local response of each disc region enhancing its damping and energy storage properties. The substitute design is based and inspired from the accurate microstructure and the most recent findings about the disc structure [20-22; 27-32], using most advanced biocompatible 3D printable materials such as hydrogel and polylactide [33-37]. The current contribution represents a first step of a very promising research point of interest about biocompatible composites that could mimic the unusual transversal and volumetric strains of the soft tissues. This would guarantee not only the same mechanical resistance of the real soft tissues as usually done but also the same natural feeling, damping movement and flexibility.

2. Material and methods

2.1. Replacement structure

The proposed design is inspired from the hierarchical structure of the natural annulus from the material scale to the lamellar/interlamellar arrangement scale. A special combination of lattice structure with octagonal cells patterns, separated by oriented fibers reinforced thin parallel sheets, is proposed as shown in Figure 1. The 3D octagonal cells shape is especially designed in order to replicate the 3D response of the natural annulus fibrosus. The special unit cell structure illustrated in Figure 2 allows an auxetic behavior (negative Poisson's ratio) in the Z direction and a standard non-auxetic behavior in the Y direction under stretching in the X

direction (equivalent to the circumferential direction of the complete disc). Note that X, Y and Z directions correspond to the circumferential, radial, axial directions of the disc. The compression of the intervertebral disc (which is the most common loading during daily activities due to body and lifted weights) leads to a tension of the annulus in the circumferential direction X of the disc. The parallel sheets give to the structure the required rigidity and govern the transversal strain in the disc axial direction. This is inspired from the real disc structural response under circumferential tension where the rigidity and the transversal behavior are principally governed by the annulus lamellae and the radial strain is mainly controlled by the interlamellar ground substance zone [20-21, 29-32, 38-39].

Two common 3D printable biocompatible materials are selected in the current replacement system as illustrated in Figure 1 for their similarities to natural tissues. Cross-linked hydrogel is selected to act as a replacement of the isotropic proteoglycan extracellular matrix. This material has excellent performance in absorption and energy storage features. The anisotropic type I collagen fibers are replaced by polylactide. This bio-polymer is used as a potential reinforcing material in recent biomechanical applications [40]. It will be used in the form of fibers for which the performance can be tailored by deformation-induced phase transformation in the vicinity of the glass transition [41-42]. The 3D printing technologies of hydrogel and polylactide fibers [33-37] have highly progressed and have become very common through the recent years. Currently, they are considered as a main pathway to functional biomedical devices, and they started to be widely used in many biomedical applications such as cartilage replacements [33-34].

2.2. Finite element model and boundary conditions

A sample of the octagonal cells replacement system of 25 mm × 10 mm × 10 mm was designed following the same specimen size defined for natural annulus specimens by

Derrouiche et al. [20]. The sample size was chosen based on the physiological dimensions of the disc and previous simulations established on annulus fibrosus circumferential specimens[1]. The geometry was implemented in MSC.Marc software and then meshed using isoparametric and arbitrarily hexahedrics 8-node meshing elements. The number of mesh elements was between 25000 and 330000 depending on the thickness of the sample. The average size of elements is 0.4 mm with refinements near contact areas between parallel the parallel sheets and the octogonal cells. An adequate element size was chosen to ensure mesh-independency. In order to reproduce the same experimental boundary conditions of the literature [17, 19, 21], the specimen is totally fixed from one side and a 10% circumferential strain is applied from the other side at a stretch rate of 4.2 min^{-1}. An illustrative example is provided in Figure 3. Different mesostructure configurations of the replacement system are considered as shown in Figure 3. Their characteristics are listed in Table 1. In a first configuration set, the cell walls thickness is varied while maintaining constant the sheets thickness. In a second configuration set, the parallel sheets thickness is varied while maintaining constant the cell walls thickness.

2.3. Microstructure-based material model

2.3.1. Kinematics

Before to present the hydrogel constitutive equations, the kinematics is briefly addressed[2]. Let us consider the hydrogel medium as a homogeneous continuum body. The mapping of the position vector $\boldsymbol{X}$ of a given material point in the initial configuration to the position vector $\boldsymbol{x} = \boldsymbol{\varphi}(\boldsymbol{X}, t)$ in the current configuration is given by the deformation gradient tensor $\mathbf{F} = \nabla_X \boldsymbol{\varphi}$

[1] The mean non-degenerate lumbar human intervertebral disc heights were found experimentally to be around 10 mm [43] and about 40 mm of anteroposterior diameter and 50 mm of transverse diameter [44]. Hence, the cross-section dimensions of our replacement system circumferential specimen were 10 mm × 10 mm, and the length was 25 mm, these values are totally physiological and represent the real dimensions of an annulus fibrosus tensile specimen. These realistic dimensions were previously adopted and validated in simulations of the real intervertebral disc annulus fibrosus [20, 29-31].

[2] The following notation is used throughout the section. Tensors and vectors are denoted by normal boldfaced letters and italicized boldfaced letters, respectively, while scalars and individual components of vectors and tensors are denoted by normal italicized letters. The superposed dot designates the time derivative.

. The time derivative of the deformation gradient tensor $\mathbf{F}$ is given by: $\dot{\mathbf{F}} = \mathbf{L}\mathbf{F}$ in which $\mathbf{L}$ is the gradient tensor of the spatial velocity $\boldsymbol{v} = \partial\boldsymbol{\varphi}/\partial t$: $\mathbf{L} = \nabla_x \boldsymbol{v}$. Introducing the notion of the intermediate configuration, the deformation gradient tensor $\mathbf{F} = \mathbf{F}_{iso}\mathbf{F}_{vol}$ can be multiplicatively split into an isochoric part $\mathbf{F}_{iso}$ and a volumetric part $\mathbf{F}_{vol}$:

$$\mathbf{F}_{iso} = J^{-1/3}\mathbf{F} \text{ and } \mathbf{F}_{vol} = J^{1/3}\mathbf{I} \tag{1}$$

in which $\mathbf{I}$ is the unit tensor and J is the Jacobian, i.e. the determinant of the deformation gradient tensor $\mathbf{F}$.

The corresponding kinematic rate can be additively decomposed as:

$$\mathbf{L} = \underbrace{\dot{\mathbf{F}}_{iso}\mathbf{F}_{iso}^{-1}}_{\mathbf{L}_{iso}} + \underbrace{\mathbf{F}_{iso}\dot{\mathbf{F}}_{vol}\mathbf{F}_{vol}^{-1}\mathbf{F}_{iso}^{-1}}_{\mathbf{L}_{vol}} \tag{2}$$

in which $\mathbf{L}_{iso}$ and $\mathbf{L}_{vol}$ are the isochoric and volumetric parts of the spatial velocity gradient tensor $\mathbf{L}$.

Using again the basic concept of the deformation gradient separation introducing the notion of the intermediate configuration, the isochoric deformation gradient tensor $\mathbf{F}_{iso}$ is further multiplicatively decomposed into an elastic part $\mathbf{F}_e$ and a viscous part $\mathbf{F}_v$:

$$\mathbf{F}_{iso} = \mathbf{F}_e\mathbf{F}_v \tag{3}$$

The elastic and viscous parts $\mathbf{L}_e$ and $\mathbf{L}_v$ of the corresponding kinematic rates additively split the velocity gradient $\mathbf{L}_{iso} = \dot{\mathbf{F}}_{iso}\mathbf{F}_{iso}^{-1}$:

$$\mathbf{L}_{iso} = \underbrace{\dot{\mathbf{F}}_e\mathbf{F}_e^{-1}}_{\mathbf{L}_e} + \underbrace{\mathbf{F}_e\dot{\mathbf{F}}_v\mathbf{F}_v^{-1}\mathbf{F}_e^{-1}}_{\mathbf{L}_v} \text{ and } \mathbf{L}_v = \underbrace{\frac{1}{2}\left(\mathbf{L}_v + \mathbf{L}_v^T\right)}_{\mathbf{D}_v} + \underbrace{\frac{1}{2}\left(\mathbf{L}_v - \mathbf{L}_v^T\right)}_{\mathbf{W}_v} \tag{4}$$

in which the viscous velocity gradient $\mathbf{L}_v$ is further additively decomposed into a viscous stretching rate $\mathbf{D}_v$ and a viscous spin rate $\mathbf{W}_v$ which drops out, i.e. $\mathbf{W}_v = \mathbf{0}$, if irrotationality

of the viscous flow is assumed[3] [45]. The evolution of the viscous deformation gradient $\mathbf{F}_v$ is then given by the relation $\dot{\mathbf{F}}_v = \mathbf{F}_e^{-1}\mathbf{D}_v\mathbf{F}_e\mathbf{F}_v$ knowing the viscous stretching rate $\mathbf{D}_v$.

2.3.2. Constitutive equations

The hydrogel free energy function $\psi_{Hydrogel}$ is additively split into a volumetric part ψ_{vol} and an isochoric part ψ_{iso} as:

$$\psi_{Hydrogel} = \psi_{iso} + \psi_{vol} \tag{5}$$

The non-linear time-dependent response of hydrogel is captured by considering the resistance to deformation as the sum of an equilibrium contribution and a time-dependent contribution deviating from the equilibrium state. The isochoric free energy function ψ_{iso} is thus given by:

$$\psi_{iso} = \psi_{eq} + \psi_{neq} \tag{6}$$

where ψ_{eq} is the equilibrium free energy function and ψ_{neq} is the non-equilibrium (viscous) free energy function.

The three free energy functions are expressed as:

$$\psi_{eq} = \frac{\mu}{2}(I_1 - 3),\ \psi_{neq} = \frac{\mu_v}{2}(I_{1e} - 3) \text{ and } \psi_{vol} = \frac{9}{2}K\left(J^{1/3} - 1\right)^2 \tag{7}$$

where μ, μ_v and K are material constants to be identified with μ the shear modulus, μ_v the viscous constant and K the bulk modulus, $I_1 = \mathrm{tr}\mathbf{C}_{iso}$ is the first strain invariant for the equilibrium part and $I_{1e} = \mathrm{tr}\mathbf{C}_e$ is the elastic first strain invariant for the viscous part. The tensors $\mathbf{C}_{iso} = \mathbf{F}_{iso}^T\mathbf{F}_{iso}$ and $\mathbf{C}_e = \mathbf{F}_e^T\mathbf{F}_e$ are, respectively, the isochoric right Cauchy-Green strain tensor and the elastic part. The evolution of the elastic deformation gradient $\mathbf{F}_e = \mathbf{F}_{iso}\mathbf{F}_v^{-1}$ is

[3] The multiplicative decomposition of the deformation gradient implies that the unloading process (relating the deformed configuration with the relaxed configuration) is not uniquely defined. Indeed, an arbitrary rigid body rotation of the relaxed configuration still leaves the relaxed configuration stress free. One way to make unique the unloaded configuration, with no loss in generality, is to assume the viscous flow irrotational.

driven by the viscous deformation gradient $\mathbf{F}_v$ that represents the obtained state during a spontaneous virtual elastic unloading to a free stress state.

The viscous stretching rate $\mathbf{D}_v$ is defined by the following general flow rule:

$$\mathbf{D}_v = \dot{\gamma}_v \frac{\boldsymbol{\sigma}'_v}{\sqrt{2}\|\boldsymbol{\sigma}_v\|}, \ \|\boldsymbol{\sigma}_v\| = \sqrt{\frac{1}{2}\mathrm{tr}\left(\boldsymbol{\sigma}'_v\boldsymbol{\sigma}'_v\right)} \tag{8}$$

where $\|\boldsymbol{\sigma}_v\|$ is the effective value of the viscous Cauchy stress $\boldsymbol{\sigma}_v$, $\boldsymbol{\sigma}'_v$ is the deviator part of $\boldsymbol{\sigma}_v$ and $\dot{\gamma}_v$ is the accumulated viscous strain rate [46]:

$$\dot{\gamma}_v = r\left|\sqrt{I_{1v}/3} - 1\right|^{-d} \|\boldsymbol{\sigma}_v\|^m \tag{9}$$

in which r, d and m are material constants to be identified and $I_{1v} = \mathrm{tr}\mathbf{B}_v$ is the viscous first strain invariant with $\mathbf{B}_v = \mathbf{F}_v\mathbf{F}_v^T$ the viscous left Cauchy-Green strain tensor.

Hydrogel sheets reinforced with polylactide fibers are described by:

$$\psi = \psi_{Hydrogel} + \psi_{Fibers} \tag{10}$$

where $\psi_{Hydrogel}$ is previously introduced in Eq. (5) and ψ_{Fibers} is expressed as follows [47-48]:

$$\psi_{Fibers} = \frac{A_1}{2A_2}\left[\exp\left(A_2\left(I_4 - 1\right)^2\right) - 1\right] + \frac{A_1}{2A_2}\left[\exp\left(A_2\left(I_6 - 1\right)^2\right) - 1\right] \tag{11}$$

where A_1 and A_2 are two fibers parameters, $I_4 = \boldsymbol{a}\mathbf{C}_{iso}\boldsymbol{a}$ and $I_6 = \boldsymbol{b}\mathbf{C}_{iso}\boldsymbol{b}$ are the fourth and sixth invariants, $\boldsymbol{a}$ and $\boldsymbol{b}$ are unitary vectors defining the orientation of two families of oriented fibers of angle θ and $-\theta$. The free energy function (11) contributes to the overall function (10) only when the superimposed fibers are in loaded in tension, i.e. $I_4 > 1$ or $I_6 > 1$, since they are inactive in compression. Note that the expression (11) may lead to an "unphysical" auxetic behavior [49]. Nonetheless, it is used to constitutively describe the thin parallel reinforced sheets for which there is no obvious auxeticity. The latter behavior is ascribed to the special configuration and geometry of the unreinforced octagonal cells described using only the expression (7).

The Cauchy stress tensor $\boldsymbol{\sigma}$ is deduced from the differentiation of the free energy functions (7) and (11) with respect to the corresponding deformations:

$$\boldsymbol{\sigma} = \underbrace{2\mathbf{F}_{iso}\frac{\partial \psi_{eq}}{\partial \mathbf{C}_{iso}}\mathbf{F}_{iso}^{T}}_{\boldsymbol{\sigma}_{e}} + \underbrace{2\mathbf{F}_{e}\frac{\partial \psi_{neq}}{\partial \mathbf{C}_{e}}\mathbf{F}_{e}^{T}}_{\boldsymbol{\sigma}_{v}} + \underbrace{\frac{\partial \psi_{vol}}{\partial J}\mathbf{I}}_{\boldsymbol{\sigma}_{vol}} + \underbrace{2\mathbf{F}_{iso}\frac{\partial \psi_{Fibers}}{\partial \mathbf{C}_{iso}}\mathbf{F}_{iso}^{T}}_{\boldsymbol{\sigma}_{Fibers}} \tag{12}$$

in which $\mathbf{C}_e = \mathbf{F}_e^T\mathbf{F}_e$ is the elastic right Cauchy-Green strain tensor.

The constitutive model has been implemented into MSC.Marc by means of a series of subroutines. Some details are provided in Appendix A.

2.3.3. Model parameters

The hydrogel model parameters were fitted to the experimental data of a P(AAm-co-AAc) nanocomposite hydrogel cross-linked by Fe^{3+} carboxyl coordination bonds extracted from [50-51]. The material system is stretched up to a level of 300% at different stretch rates in the equilibrated and fully swollen state. The rate-dependence and the hysteresis upon a loading-retraction cycle are perfectly reproduced by the constitutive model as illustrated in Figure 3. The polylactide material parameters were identified using the experimental data of a polylactide fiber extracted from the work of Cicero and Dorgan [52]. The material parameters of the constituent elements are listed in Table 2.

3. Results

The mechanics of the new designs is examined as a function both of its mesostructure in terms of cell walls/sheets thickness and of its microstructure in terms of fibers orientation.

3.1. Mesostructure

The mechanics of the replacement system are reported in Figure 5 considering different mesostructure configurations for fibers orientation θ =±30°. The in-silico results are

compared with available experimental data obtained on annulus specimens of the human lumbar intervertebral disc. The experimental stress-strain results are those of Ebara et al. [17] and the experimental transversal strain results are those of Baldit et al. [19]. It is very satisfactory to observe that the substitute systems can reproduce the nonlinear stiffness and transversal strains of the natural annulus with auxetic response in the radial direction and unusual response with Poisson's ratios higher than 0.5 in the axial direction. It can be observed that the mechanics is not monotonically dependent on the thickness. The increase in thickness decreases the stiffness but the effect on the transversal strains is very slight. Only the transversal response of the W0.2-S0.2 design slightly diverges from the other configurations when the applied circumferential strain exceeds 0.6.

3.2. Microstructure

As observed in Figure 6, the replacement system is able to reproduce perfectly the mechanics of the local annulus specimen. The auxeticity increases when the fibers angle decreases, and the axial strain increases when the fibers angle increases. By varying the orientation of the polylactide fibers, both nonlinear stiffness and transversal behavior, can be modified in the aim to mimic the exact response of the different radial and circumferential regions of the natural annulus reported experimentally in Ebara et al. [17]. This important result makes it possible to foresee the possibility of designing a complete prosthetic of the disc with gradual variation in local properties and even the creation of personalized tissue-engineered discs.

4. Discussion

The design of an annulus fibrosus artificial substitute that could perfectly mimic the natural annulus mechanics is a challenging task due to the complexity of the disc tissue hierarchic structure and its unusual transverse response along with regional dependency. However, the

challenge was accepted by many researchers in the recent years [53-54] and it was hence the main objective of the current contribution. A new annulus replacement system, inspired from the real structure of the natural disc, is designed and implemented in-silico in order to be numerically tested. The system is composed of reinforced parallel sheets separated by a lattice structure with octagonal cells patterns. This configuration permits for the first time reproducing accurately not only the nonlinear stiffness of the annulus [55] but also its volumetric response [19-22]. This specific structure optimizes also the consumed material and highly reduces the elaboration cost which is of prime interest since the hydrogel, used as the ground matrix of the designed system, is very expensive. As seen in the simulation results, the system response could be highly controlled by the reinforcing fibers and slightly controlled by the mesostructure thickness. This allows changing the local response of the different annulus regions when constructing a complete prosthetic and permits reproducing the correct regional dependency of the natural disc. It could be thus improved to create advanced personalized replacements. The material choice is very large but as seen in the current contribution, the use of biocompatible materials, such as hydrogel and polylactide fibers, is always essential for biomedical applications [56-58]. Hydrogel is known to present many mechanical similarities with the human tissues and polylactide is identified as a biodegradable material that starts to be widely used in biomedicine [59-60]. The possibility of printing those two materials via the most recent 3D printing technologies would simplify the manufacturing of such innovative structures [61-63].

In the current paper, a specimen of the new substitute system was designed replicating the same form and dimensions of experimental specimens in the literature and tested under tension loading in the circumferential direction of the intervertebral disc. The system succeeded to reproduce the same physiological nonlinear stiffness of the real annulus. What is very interesting is the ability of the system to reproduce the exact stress-strain response of the

different intervertebral disc regions. The hydrogel octagonal cells patterns succeed to give the replacement structure the auxetic feature and mimic the correct nonlinear annulus fibrosus radial strain and the radial swelling. Reinforced by the oriented polylactide fibers the parallel sheets shrink axially giving the substitute the natural particular Poisson's ratio higher than 0.5 of the real annulus. The mesostructure (cell walls or parallel sheets) would affect the scaffold response but the effect is negligible compared to the effect of the different constituent elements, in particular the fibers orientation.

5. Conclusion

A novel hydrogel-based annulus fibrosus substitute system is designed, constructed in-silico and numerically tested. The special structure, bio-inspired from the natural annulus lamellar/interlamellar arrangement, is tailored by the lattice structure and the fibers orientation. It succeeds to mimic accurately the nonlinear stiffness and the transversal behavior of the different annulus regions. By using 3D printable biocompatible materials such as hydrogel and polylactide fibers to construct our system, a complete heterogeneous annulus could be created. In addition, the system permits manufacturing personalized tissue-engineered discs miming the mechanics of each individual and each disc level which will be the objective of the following steps of the project.

The verification of the capabilities of our systems to mimic the multiaxial mechanics of the natural annulus remains an important issue [30, 39]. In this regard, the constitutive representation of the hydrogel will be enriched in future works, especially to get out of the limitations of the used free energy functions vis-à-vis their predictive capabilities upon multiaxial loading [64]. More sophisticated expressions will be used to accurately describe the multiaxial characteristics of our systems in connection to loading history and hydrogel microstructure [65-66].

Appendix A. Numerical implementation

The constitutive model affected to the replacement system is implemented into MSC.Marc software by means of a series of subroutines. The reader is also referred to complementary references [29, 67-68] for the general implementation procedure of coupled models. An anisotropic hyperelastic subroutine is here coupled to a viscous subroutine. A total Lagrange formulation was adopted for the present calculations. When the total Lagrange is selected, MSC.Marc software deals with the second Piola-Kirchhoff stress $\mathbf{S}$ and the Green-Lagrange strain $\mathbf{E}$. An updated Lagrange formulation could be also used and in that case the software would deal with the Cauchy stress $\boldsymbol{\sigma}$ and the logarithmic strain $\ln(\mathbf{F})$.

A.1. The anisotropic hyperelastic subroutine

The deformation gradient $\mathbf{F}(i)$ is computed at the beginning of each increment by [69]:

$$\mathbf{F}(i)=\exp\left(\ln\left(\mathbf{F}(i)\right)\right)=\sum_{j=0}^{\infty}\frac{1}{j!}\left(\ln\left(\mathbf{F}(i)\right)\right)^{(j)} \tag{A1}$$

where $\ln\left(\mathbf{F}(i)\right)$ is given by the numerical code.

The identification of the elastic strain energy function and its derivatives with respect to the volume preserving parts of the first invariant $\tilde{I}_1$, the second invariant $\tilde{I}_2$, the fourth invariant $\tilde{I}_4$ and the sixth invariant $\tilde{I}_6$ are required by the hyperelastic subroutine as follows:

$$\left\{\psi_{dev}(i);\frac{\partial\psi(i)}{\partial\tilde{I}_1};\frac{\partial\psi(i)}{\partial\tilde{I}_2};\frac{\partial\psi(i)}{\partial\tilde{I}_4};\frac{\partial\psi(i)}{\partial\tilde{I}_6}\right\} \tag{A2}$$

where $\psi(i)=\psi_{dev}(i)+u(i)$ defined for the parallel sheets as:

$$\psi_{dev}(i)=\psi_{Hydrogel}(i)+\psi_{Fibers}(i) \text{ and } u(i)=\psi_{vol}(i) \tag{A3}$$

and for the octagonal cell as:

$$\psi_{dev}(i)=\psi_{Hydrogel}(i) \text{ and } u(i)=\psi_{vol}(i) \tag{A4}$$

After the definition of the strain energy function and the derivatives, the software defines the elastic second Piola-Kirchhoff stress and the volumetric stress for the parallel sheets as:

$$\mathbf{S}_e(i)=2\frac{\partial\psi_{eq}(i)+\partial\psi_{Fibers}(i)}{\partial\mathbf{C}_{iso}(i)} \text{ and } \mathbf{S}_{vol}(i)=J^{1/3}\frac{\partial u(i)}{\partial J} \tag{A5}$$

and for the octogonal cells as:

$$\mathbf{S}_e(i)=2\frac{\partial\psi_{eq}(i)}{\partial\mathbf{C}_{iso}(i)} \text{ and } \mathbf{S}_{vol}(i)=J^{1/3}\frac{\partial u(i)}{\partial J} \tag{A6}$$

A.2. The viscous subroutine

To compute the current elastic deformation gradient $\mathbf{F}_e(i)$, the viscous deformation gradient $\mathbf{F}_v(i-1)$ user-stored from the previous increment is called:

$$\mathbf{F}_e(i)=\mathbf{F}_{iso}(i)\mathbf{F}_v(i-1)^{-1} \tag{A7}$$

The calculated elastic deformation gradient $\mathbf{F}_e(i)$ is then used to calculate the viscous velocity gradient $\mathbf{L}_v(i)=\mathbf{D}_v(i)$ with $\mathbf{D}_v(i)$ the viscous stretching rate at the end of the current increment. The rate of the viscous deformation gradient writes:

$$\dot{\mathbf{F}}_v(i)=\mathbf{F}_e(i)^{-1}\mathbf{D}_v(i)\mathbf{F}_{iso}(i) \tag{A8}$$

The current viscous deformation gradient $\mathbf{F}_v(i)$ is iteratively calculated using:

$$\mathbf{F}_v(i)=\dot{\mathbf{F}}_v(i)\Delta t+\mathbf{F}_v(i-1) \tag{A9}$$

where Δt is the time increment.

At the beginning of the mechanical loading, the singularity of the viscous stretching rate is avoided by adding a perturbation coefficient κ =0.01 to $\sqrt{I_{1v}/3}$. The value of $\mathbf{F}_v(i)$ is user-

stored in the form of a 3-D matrix $[m, nn, p]$ constituted of *m* number of elements, *nn* number of nodes and *p* number of tensor directions.

The strain invariants are calculated from the Cauchy-Green deformation components in order to be used next in the stress calculation. The non-equilibrium (viscous) stress is calculated in the subroutine by the following expression:

$$\mathbf{S}_v(i) = 2\frac{\partial \psi_{neq}(i)}{\partial \mathbf{C}_e} \tag{A10}$$

Finally, the elastic and volumetric stresses are called from the hyperelastic subroutine, and the total second Piola-Kirchhoff stress is calculated by the summation of the different stress components:

$$\mathbf{S}(i) = \mathbf{S}_e(i) + \mathbf{S}_v(i) + \mathbf{S}_{vol}(i) \tag{A11}$$

References

[1] Galbusera, F, Bellini, C.M., Brayda-Bruno, M., Fornari, M. Biomechanical studies on cervical total disc arthroplasty: a literature review. Clinical Biomechanics 2008;23:1095-1104.

[2] Amoretti, N., Iannessi, A., Lesbats, V., Marcy, P.Y., Hovorka, E., Bronsard, N., Fonquerne, M.E., Hauger, O. Imaging of intervertebral disc prostheses. Diagnostic and Interventional Imaging 2012;93:10-21.

[3] Jiang, Q., Zaïri, F., Frederix, C., Derrouiche, A., Yan, Z., Qu, Z., Liu, X., Zaïri, F. Crystallinity dependency of the time-dependent mechanical response of polyethylene: application in total disc replacement. Journal of Materials Science: Materials in Medicine 2019;30:46.

[4] Jiang, Q., Zaïri, F., Frederix, C., Yan, Z., Derrouiche, A., Qu, Z., Liu, X., Zaïri, F. Biomechanical response of a novel intervertebral disc prosthesis using functionally graded polymers: a finite element study. Journal of the Mechanical Behavior of Biomedical Materials 2019;94:288-297.

[5] Jacobs, C. A. M., Siepe, C. J., Ito, K. Viscoelastic cervical total disc replacement devices: Design concepts. The Spine Journal 2020;20:1911-1924.

[6] Giancarlo Vishteh, A., Dickman, C.A. Anterior lumbar microdiscectomy and interbody fusion for the treatment of recurrent disc herniation. Neurosurgery 2001;48:334-338.

[7] Van Ooij, A., Oner, F.C., Verbout, A.J. Complications of artificial disc replacement: a report of 27 patients with the SB Charite disc. Spine 2003;28:369-383.

[8] Zechmeister, I., Winkler, R., Mad, P. Artificial total disc replacement versus fusion for the cervical spine: a systematic review. European Spine Journal 2011;20:177-184.

[9] Lopez, C.D., Boddapati, V., Lombardi, J.M., Lee, N.J., Saifi, C., Dyrszka, M.D., Sardar, Z.M., Lenke, L.G., Lehman, R.A. Recent trends in medicare utilization and reimbursement for lumbar spine fusion and discectomy procedures. The Spine Journal 2020;20:1586-1594.
[10] Lazennec, J. Y., Aaron, A., Ricart, O., Rakover, J.P. The innovative viscoelastic CP ESP cervical disk prosthesis with six degrees of freedom: biomechanical concepts, development program and preliminary clinical experience. European Journal of Orthopaedic Surgery & Traumatology 2016;26:9-19.
[11] Patwardhan, A.G., Tzermiadianos, M. N., Tsitsopoulos, P.P., Voronov, L.I., Renner, S. M., Reo, M.L., Carandang, G., Ritter-Lang, K., Havey, R. M. Primary and coupled motions after cervical total disc replacement using a compressible six-degree-of-freedom prosthesis. European Spine Journal 2012;21:618-629.
[12] Thomas, S., Willems, K., van den Daelen, L., Linden, P., Ciocci, M.C., Bocher, P. The M6-C cervical disk prosthesis: first clinical experience in 33 patients. Clinical Spine Surgery 2016;29:E182-E187.
[13] Patwardhan, A.G., Havey, R.M. Prosthesis design influences segmental contribution to total cervical motion after cervical disc arthroplasty. European Spine Journal 2019;29:2713-2721.
[14] Eyre, D.R., Muir, H. Types I and II collagens in intervertebral disc. Interchanging radial distributions in annulus fibrosus. Biochemical Journal 1976;157:267-270.
[15] Eyre, D.R., Muir, H. Quantitative analysis of types I and II collagens in the human intervertebral discs at various ages. Biochimica Biophysica Acta 1977;492:29-42.
[16] Skaggs, D.L., Weidenbaum, M., Iatridis, J. C., Ratcliffe, A., Mow, V.C. Regional variation in tensile properties and biochemical composition of the human lumbar anulus fibrosus. Spine 1994;19:1310-1319.
[17] Ebara, S., Iatridis, J.C., Setton, L.A., Foster, R.J., Mow, V.C., Weidenbaum, M. Tensile properties of nondegenerate human lumbar anulus fibrosus. Spine 1996;21:452-461.
[18] Holzapfel, G.A., Schulze-Bauer, C.A.J., Feigl, G., Regitnig, P. Single lamellar mechanics of the human lumbar. Biomechanics and Modeling in Mechanobiology 2005;3:125-140.
[19] Baldit, D., Ambard, D., Cherblanc, F., Royer, P. Experimental analysis of the transverse mechanical behaviour of annulus fibrosus tissue. Biomechanics and Modeling in Mechanobiology 2014;13:643-652.
[20] Derrouiche, A., Zaïri, F., Zaïri, F. A chemo-mechanical model for osmo-inelastic effects in the annulus fibrosus. Biomechanics and Modeling in Mechanobiology 2019;18:1773-1790.
[21] Derrouiche, A., Karoui, A., Zaïri, F., Ismail, J., Qu, Z., Chaabane, M., Zaïri, F. The two Poisson's ratios in annulus fibrosus: relation with the osmo-inelastic features. Mechanics of Soft Materials 2020;2:1.
[22] Dusfour, G., LeFloc'h, S., Canadas, P., Ambard, D. Heterogeneous mechanical hyperelastic behavior in the porcine annulus fibrosus explained by fiber orientation: an experimental and numerical approach. Journal of the Mechanical Behavior of Biomedical Materials 2020;104:103672.
[23] Nerurkar, N. L., Baker, B. M., Sen, S., Wible, E.E., Elliott, D.M., Mauck, R.L. Nanofibrous biologic laminates replicate the form and function of the annulus fibrosus. Nature Materials 2009;8:986-992.
[24] Du, L., Yang, Q., Zhang, J., Zhu, M., Ma, X., Zhang, Y., Wang, L., Xu, B. Engineering a biomimetic integrated scaffold for intervertebral disc replacement. Materials Science and Engineering: C 2019;96:522-529.

[25] Frost, B.A., Foster, E.J. Replication of annulus fibrosus through fabrication and characterization of polyurethane and cellulose nanocrystal composite scaffolds. Nanocomposites 2019;5:13-27.
[26] Bhunia, B.K., Dey, S., Bandyopadhyay, A., Mandal, B.B. 3D printing of annulus fibrosus anatomical equivalents recapitulating angle-ply architecture for intervertebral disc replacement. Applied Materials Today 2021;23:101031.
[27] Tavakoli, J., Costi, J.J. New findings confirm the viscoelastic behaviour of the inter-lamellar matrix of the disc annulus fibrosus in radial and circumferential directions of loading. Acta Biomaterialia 2018;71:411-419.
[28] Tavakoli, J., Elliott, D.M., Costi, J.J. The ultra-structural organization of the elastic network in the intra- and inter-lamellar matrix of the intervertebral disc. Acta Biomaterialia 2017;58:269-277.
[29] Kandil, K., Zaïri, F., Derrouiche, A., Messager, T., Zaïri, F. Interlamellar-induced time-dependent response of intervertebral disc annulus: a microstructure-based chemo-viscoelastic model. Acta Biomaterialia 2019;100:75-91.
[30] Kandil, K., Zaïri, F., Messager, T., Zaïri, F. Interlamellar matrix governs human annulus fibrosus multiaxial behavior. Scientific Reports 2020;10:19292.
[31] Kandil, K., Zaïri, F., Messager, T., Zaïri, F. A microstructure-based modeling approach to assess aging-sensitive mechanics of human intervertebral disc. Computer Methods and Programs in Biomedicine 2021;200:105890.
[32] Tamoud, A., Zaïri, F., Mesbah, A., Zaïri, F. A microstructure-based model for time-dependent mechanics of multi-layered soft tissues and its application to intervertebral disc annulus. Meccanica 2021;56:585-606.
[33] Bakarich, S.E., Gorkin III, R., in het Panhuis, M., Spinks, G.M., 2014. Three-dimensional printing fiber reinforced hydrogel composites. ACS Applied Materials & Interfaces 2014;6:15998-16006.
[34] Bakarich, S.E., Gorkin III, R., Naficy, S., Gately, R., in het Panhuis, M., Spinks, G.M. 3D/4D printing hydrogel composites: a pathway to functional devices. MRS Advances 2016;1:521-526.
[35] Bakarich, S.E., Gorkin III, R., Gately, R., Naficy, S., in het Panhuis, M., Spinks, G.M. 3D printing of tough hydrogel composites with spatially varying materials properties. Additive Manufacturing 2017;14:24-30.
[36] Wang, X., Jiang, M., Zhou, Z., Gou, J., Hui, D. 3D printing of polymer matrix composites: a review and prospective. Composites Part B: Engineering 2017;110:442-458.
[37] Herman, K., Torres, G., Yokoyama, K., Gallippi, C. M. Elastically anisotropic phantoms constructed from 3D-printed PLA fibers. IEEE International Ultrasonics Symposium (IUS) 2020;1-3.
[38] Kandil, K., Zaïri, F., Messager, T., Zaïri, F. A microstructure-based model for a full lamellar-interlamellar displacement and shear strain mapping inside human intervertebral disc core. Computers in Biology and Medicine 2021;104629.
[39] Tamoud, A., Zaïri, F., Mesbah, A., Zaïri, F. A multiscale and multiaxial model for anisotropic damage and failure of human annulus fibrosus. International Journal of Mechanical Sciences 2021;106558.
[40] Critchley, S., Sheehy, E.J., Cunniffe, G., Diaz-Payno, P., Carroll, S.F., Jeon, O., Alsberg, E., Brama, P.A.J., Kelly, D.J. 3D printing of fibre-reinforced cartilaginous tem- plates for the regeneration of osteochondral defects. Acta Biomaterialia 2020;113:130-143.
[41] Mahjoubi, H., Zaïri, F., Tourki, Z. A micro-macro constitutive model for strain-induced molecular ordering in biopolymers: application to polylactide over a wide range of temperatures. International Journal of Plasticity 2019;123:38-55.

[42] Mahjoubi, H., Zaïri, F., Tourki, Z. Strain-induced phase transformation in poly (lactic acid) across the glass transition: Constitutive model and identification. International Journal of Non-Linear Mechanics 2020;118:103241.
[43] Roberts, N., Gratin, C., Whitehouse, G.H. MRI analysis of lumbar intervertebral disc height in young and older populations. Journal of Magnetic Resonance Imaging 1997;7:880-886.
[44] Wang, Y., Battié, M.C., Videman, T. A morphological study of lumbar vertebral endplates: radiographic, visual and digital measurements. European Spine Journal 2012;21:2316-2323.
[45] Gurtin, M.E., Anand, L. The decomposition $F = F_eF_p$, material symmetry, and plastic irrotationality for solids that are isotropic-viscoplastic or amorphous. International Journal of Plasticity 2005;21:1686-1719.
[46] Bergstrom, J.S., Boyce, M.C. Constitutive modeling of the large strain time-dependent behavior of elastomers. Journal of the Mechanics and Physics of Solids 1998;46:931-954.
[47] Holzapfel, G.A., Gasser, T.C., Ogden, R.W. A new constitutive framework for arterial wall mechanics and a comparative study of material models. Journal of Elasticity and the Physical Science of Solids 2000;61:1-48.
[48] Holzapfel, G.A., Gasser, T.C. A viscoelastic model for fiber-reinforced composites at finite strains: Continuum basis, computational aspects and applications. Computer Methods in Applied Mechanics and Engineering 2001;190:4379-4403.
[49] Skacel, P., Bursa, J. Poisson's ratio of arterial wall – Inconsistency of constitutive models with experimental data. Journal of the Mechanical Behavior of Biomedical Materials 2016;54:316-327.
[50] Zheng, S.Y., Ding, H., Qian, J., Yin, J., Wu, Z.L., Song, Y., Zheng, Q. Metal-coordination complexes mediated physical hydrogels with high toughness, stick–slip tearing behavior, and good processability. Macromolecules 2016;49:9637-9646.
[51] Lin, J., Zheng, S.Y., Xiao, R., Yin, J., Wu, Z.L., Zheng, Q., Qian, J. Constitutive behaviors of tough physical hydrogels with dynamic metal-coordinated bonds. Journal of the Mechanics and Physics of Solids 20201;39:103935.
[52] Cicero, J.A., Dorgan, J.R. Physical properties and fiber morphology of poly (lactic acid) obtained from continuous two-step melt spinning. Journal of Polymers and the Environment 2001;9:1-10.
[53] Nerurkar, N.L., Baker, B.M., Sen, S., Wible, E.E., Elliott, D.M., Mauck, R. L. Nanofibrous biologic laminates replicate the form and function of the annulus fibrosus. Nature Materials 2009;8:986-992.
[54] Pereira, D.R., Silva-Correia, J., Oliveira, J.M., Reis, R. L., Pandit, A., Biggs, M.J. Nanocellulose reinforced gellan-gum hydrogels as potential biological substitutes for annulus fibrosus tissue regeneration. Nanomedicine: Nanotechnology, Biology and Medicine 2018;14:897-908.
[55] Ambard, D., Cherblanc, F. Mechanical behavior of annulus fibrosus: a microstructural model of fibers reorientation. Annals of Biomedical Engineering 2009;37:2256-2265.
[56] Noguchi, T., Yamamuro, T., Oka, M., Kumar, P., Kotoura, Y., Hyonyt, S. H., Ikadat, Y. Poly(vinyl alcohol) hydrogel as an artificial articular cartilage: evaluation of biocompatibility. Journal of Applied Biomaterials 1991;2:101-107.
[57] Ramot, Y., Haim-Zada, M., Domb, A. J., Nyska, A. Biocompatibility and safety of PLA and its copolymers. Advanced Drug Delivery Reviews 2016;107:153-162.
[58] Naahidi, S., Jafari, M., Logan, M., Wang, Y., Yuan, Y., Bae, H., Dixon, B., Chen, P. Biocompatibility of hydrogel-based scaffolds for tissue engineering applications. Biotechnology Advances 2017;35:530-544.

[59] Asghari, F., Samiei, M., Adibkia, K., Akbarzadeh, A., Davaran, S. Biodegradable and biocompatible polymers for tissue engineering application: a review. Artificial cells, Nanomedicine, and Biotechnology 2017;45:185-192.
[60] da Silva, D., Kaduri, M., Poley, M., Adir, O., Krinsky, N., Shainsky-Roitman, J., Schroeder, A. Biocompatibility, biodegradation and excretion of polylactic acid (PLA) in medical implants and theranostic systems. Chemical Engineering Journal 2018;340:9-14.
[61] Wei, J., Wang, J., Su, S., Wang, S., Qiu, J., Zhang, Z., Christopher, G., Ning, F., Cong, W. 3D printing of an extremely tough hydrogel. RSC Advances 2015;5:81324-81329.
[62] Hong, S., Sycks, D., Chan, H. F., Lin, S., Lopez, G. P., Guilak, F., Leong, K.W., Zhao, X. 3D printing of highly stretchable and tough hydrogels into complex, cellularized structures. Advanced Materials 2015;27:4035-4040.
[63] Chen, Z., Zhao, D., Liu, B., Nian, G., Li, X., Yin, J., Qu, S., Yang, W. 3D printing of multifunctional hydrogels. Advanced Functional Materials 2019;29:1900971.
[64] Amores, V.J., Nguyen, K., Montans, F.J. On the network orientational affinity assumption in polymers and the micro-macro connection through the chain stretch. Journal of the Mechanics and Physics of Solids 2021;148:104279.
[65] Guo, Q., Zaïri, F. A micromechanics-based model for deformation-induced damage and failure in elastomeric media. International Journal of Plasticity 2021;140:102976.
[66] Saadedine, M., Zaïri, F., Ouali, N., Tamoud, A., Mesbah, A. A micromechanics-based model for visco-super-elastic hydrogel-based nanocomposites. International Journal of Plasticity 2021;144:2021, 103042.
[67] Ovalle-Rodas, C., Zaïri, F., Naït-Abdelaziz, M., Charrier, P. A thermo-visco-hyperelastic model for the heat build-up during low-cycle fatigue of filled rubbers: formulation, implementation and experimental verification. International Journal of Plasticity 2016;79: 217-236.
[68] Guo, Q., Zaïri, F., Guo, X. A thermo-viscoelastic-damage constitutive model for cyclically loaded rubbers. Part I: model formulation and numerical examples. International Journal of Plasticity 2018;101:106-124.
[69] de Souza Neto, E.A., Peric, D., Owen, D.R.J., 2008. Computational Methods for Plasticity: Theory and Applications, John Wiley and Sons Publication.

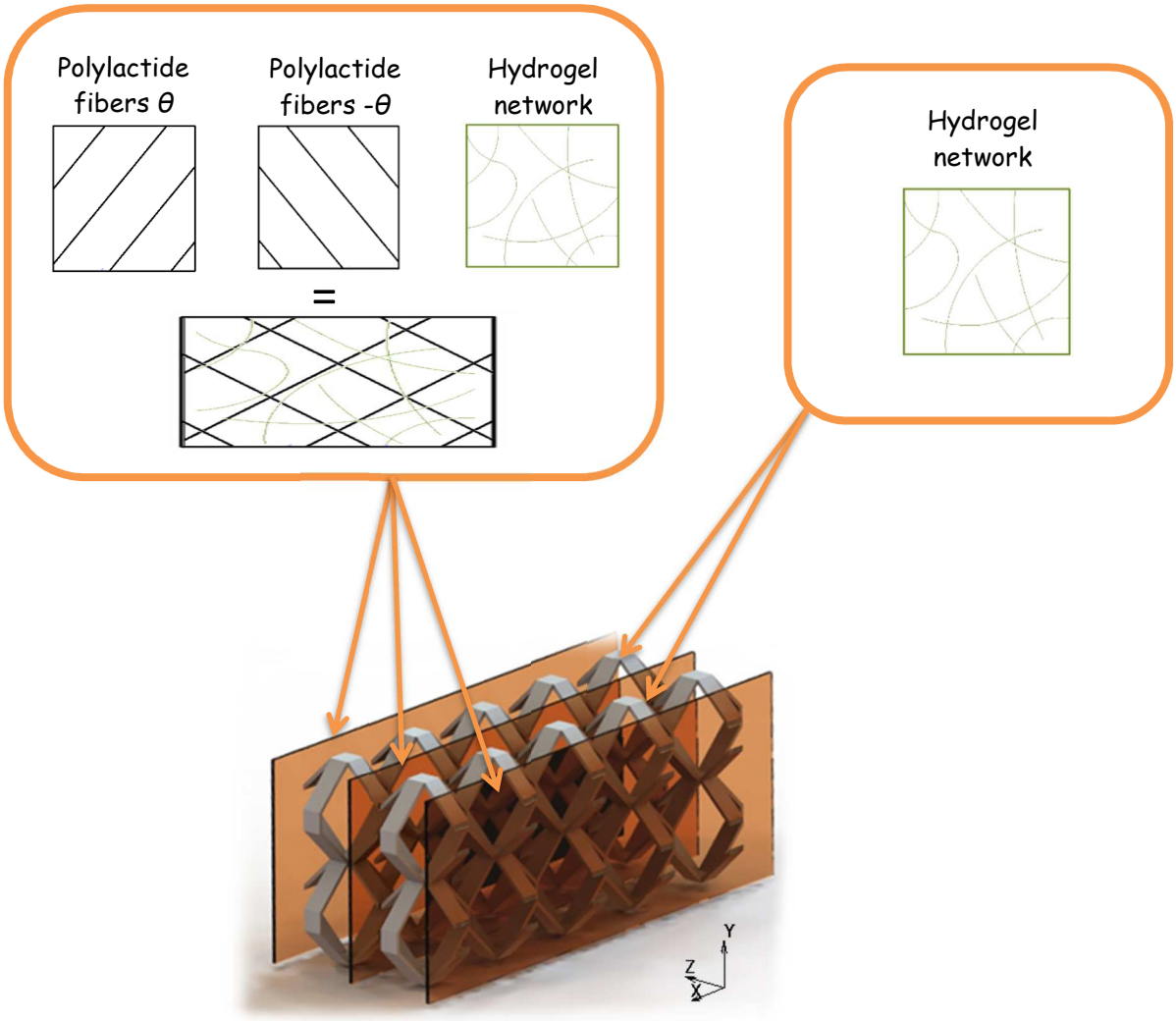

Figure 1. Hydrogel-based annulus replacement system consisting in a lattice structure with special octagonal cells and parallel thin sheets reinforced by oriented polylactide fibers.

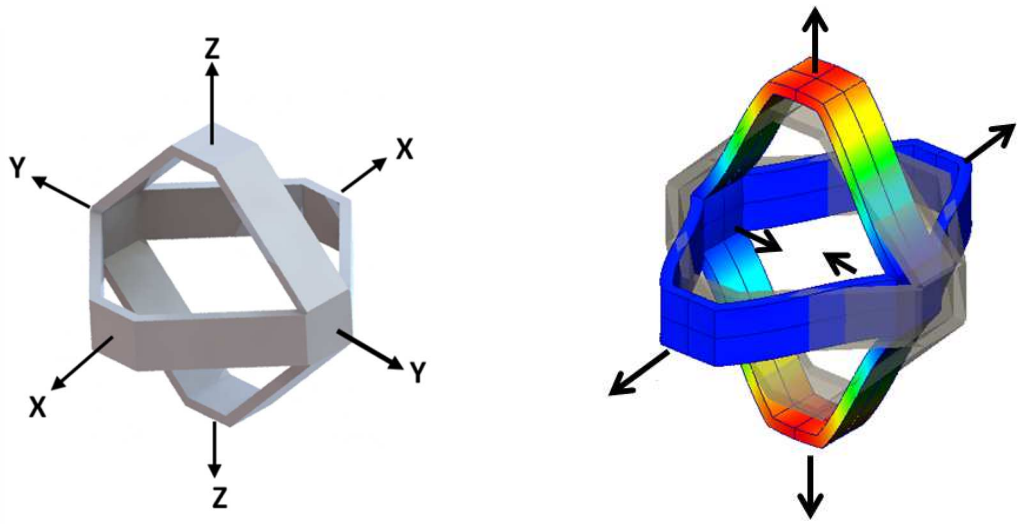

Figure 2. Special octagonal unit cell exhibiting an auxetic deformation in the Z direction and an ordinary non-auxetic deformation in the Y direction in the course of deformation along the X direction.

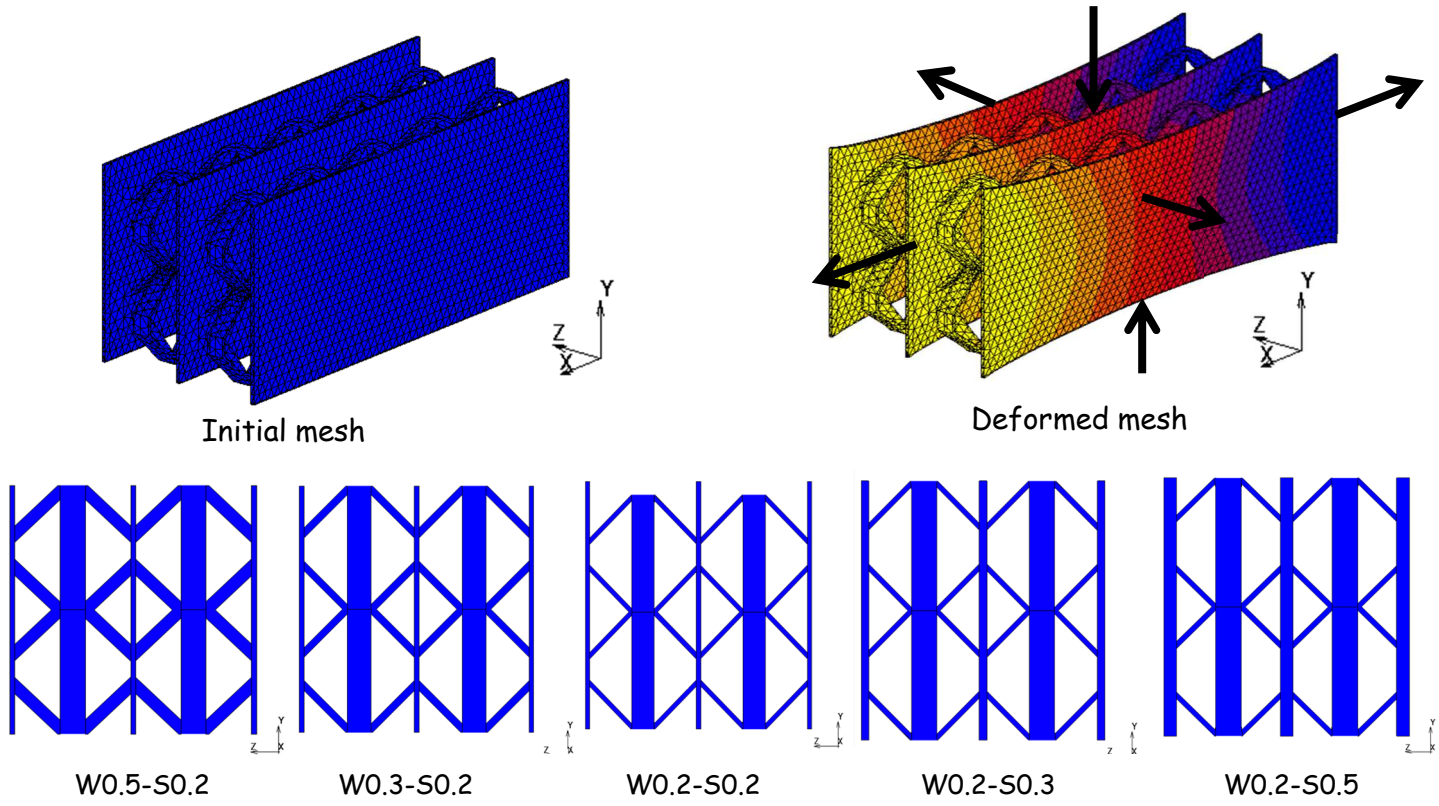

Figure 3. Mesh of the annulus replacement system and deformed mesh showing an auxetic deformation in the Z direction and an ordinary non-auxetic deformation in the Y direction in the course of deformation along the X direction. Different mesostructure configurations are considered to tailor the transverse deformations in the Y and Z directions.

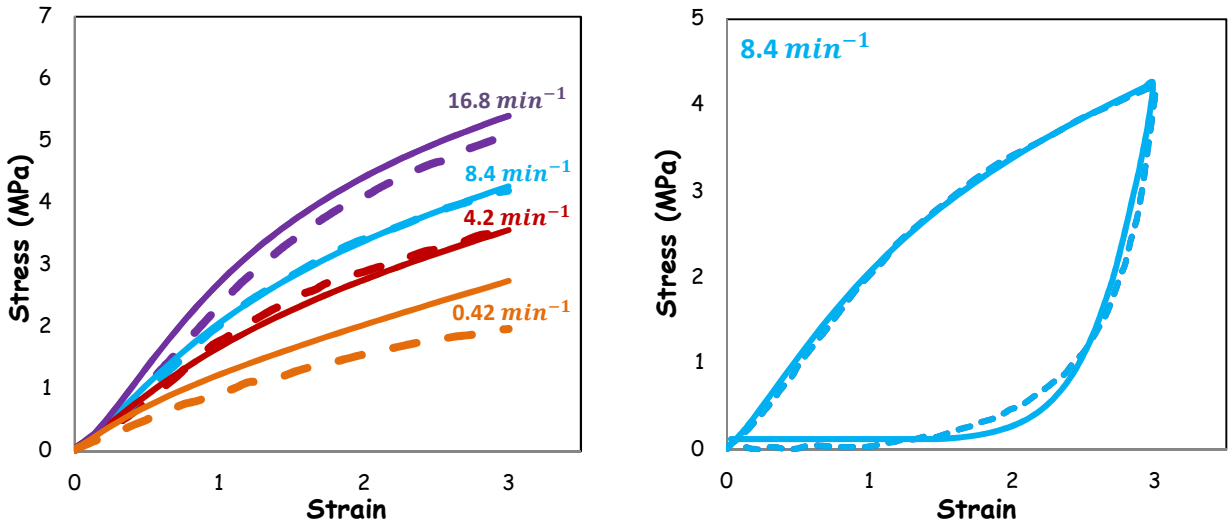

(a) (b)

Figure 4. Model fitting to capture (a) the rate-dependent engineering stress-strain response and (b) the engineering stress hysteretic response of a hydrogel (solid lines: model, dashed lines: experiments extracted from [50-51]).

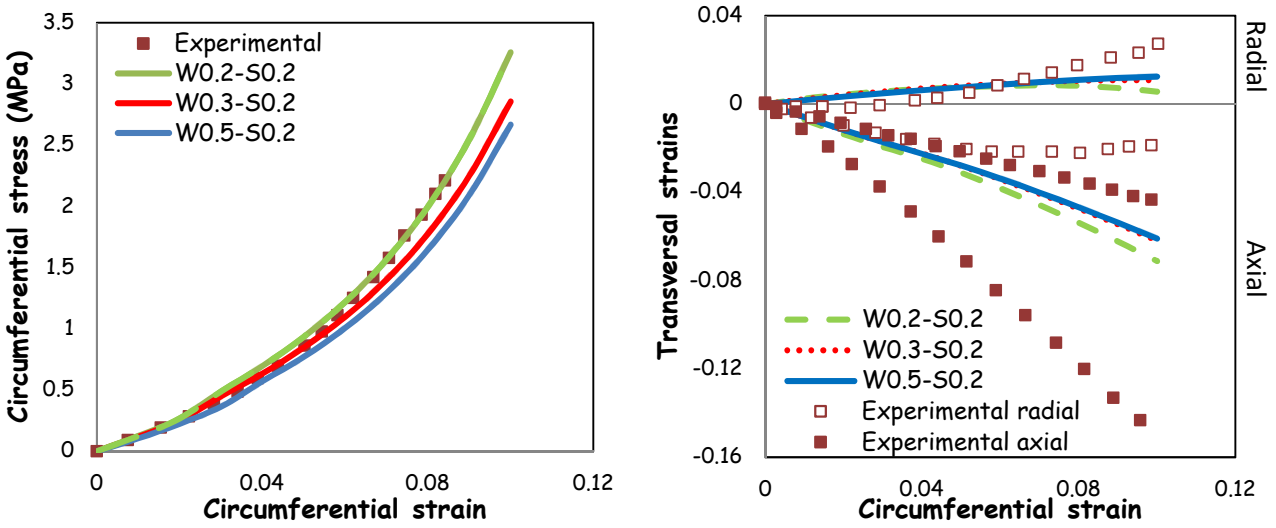

(a)

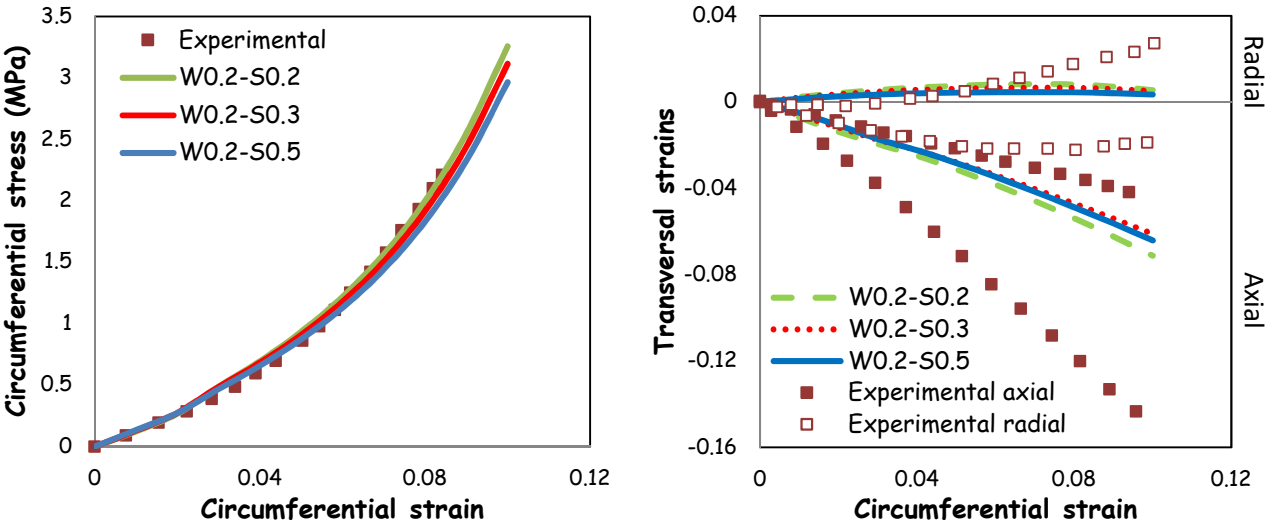

(b)

Figure 5. Mesostructure effects on nonlinear stiffness and transversal strain history in axial/radial directions: (a) cell walls thickness and (b) sheets thickness. The experimental stress-strain data are extracted from [17] and correspond to the anterior outer disc region; the experimental transversal strain data correspond to the extremum values reported in [19].

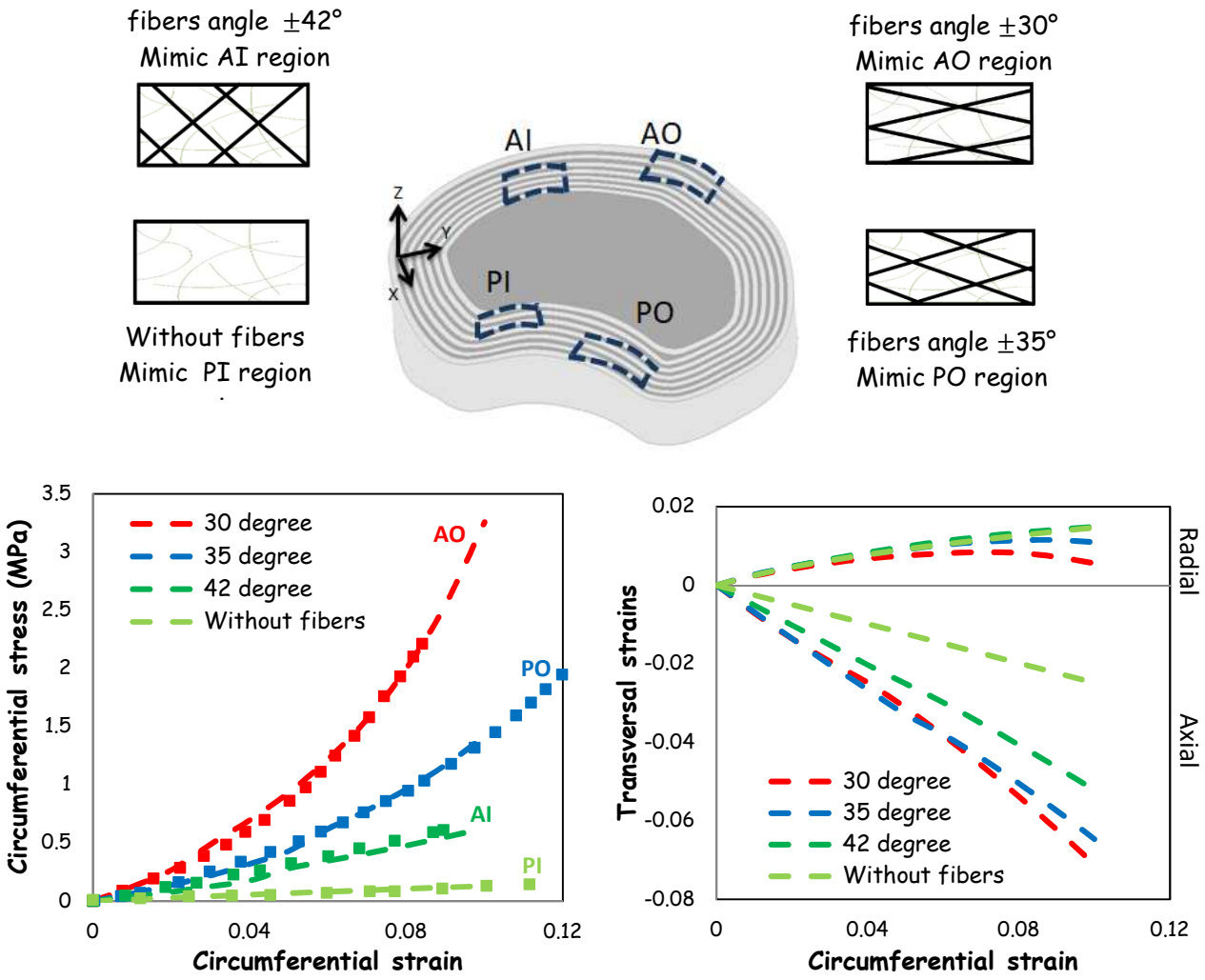

Figure 6. Fibers angle variation to mimic the regional variation in nonlinear stiffness and transversal behavior of the natural annulus. The square symbols correspond to the four disc regions extracted from the experiments of Ebara et al. [17]: Anterior outer (AO), Anterior inner (AI), Posterior outer (PO) and Posterior inner (PI). The illustrative example is for the configuration W0.2-S0.2.

	W0.5-S0.2	W0.3-S0.2	W0.2-S0.2	W0.2-S0.3	W0.2-S0.5
Cell walls thickness (mm)	0.5	0.3	0.2	0.2	0.2
Parallel sheets thickness (mm)	0.2	0.2	0.2	0.3	0.5

Table 1. Different mesostructure configurations of the annulus replacement system.

Hydrogel	μ	0.33 MPa
	μ_v	30 MPa
	K	2200 MPa
	m	1.2
	d	1.5
	r	0.008 MPa/s
Polylactide fibers	A_1	6 MPa
	A_2	58

Table 2. Parameters of the constituent elements.

Real lamellar/interlamellar annulus structure

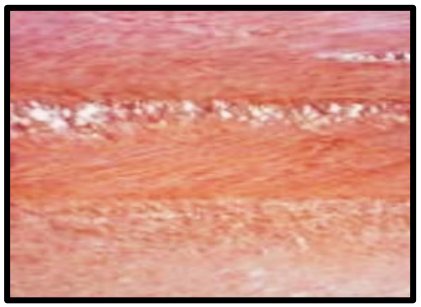

Replacement system

Replication of the natural behavior

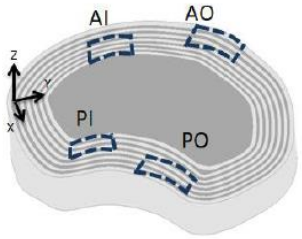

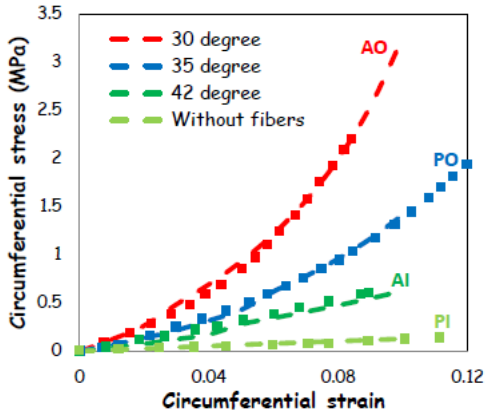

Regional-dependent non-linear stiffness

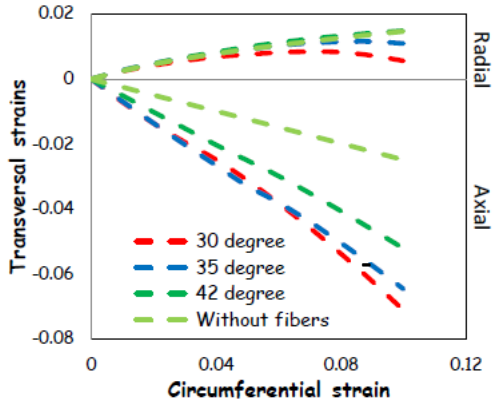

Regional-dependent transversal strain

Resulted response

New design

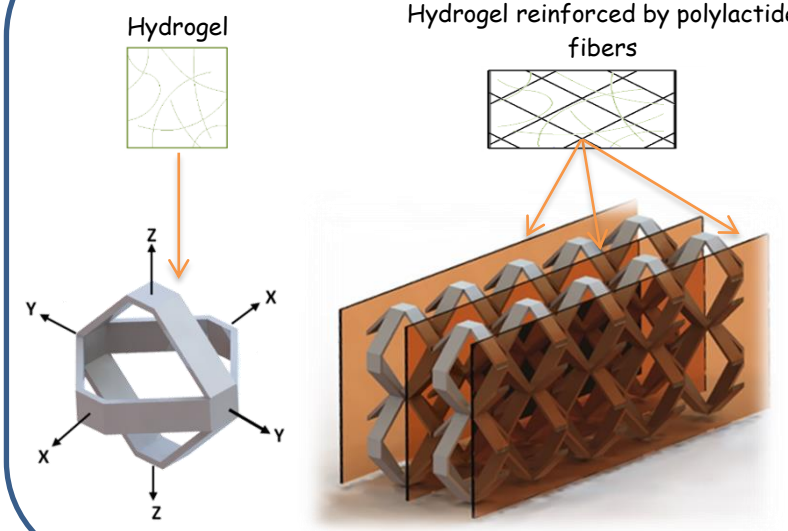

FE computations

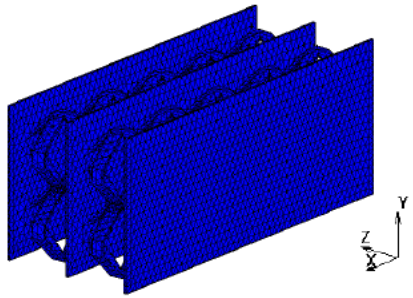

Initial mesh

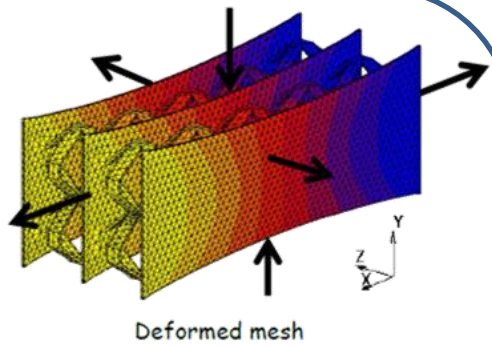

Deformed mesh

After deformation

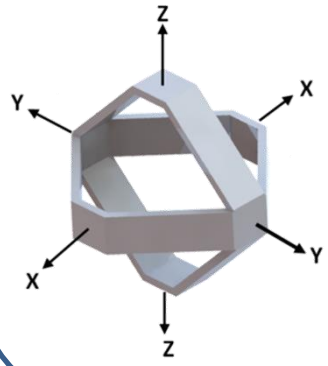

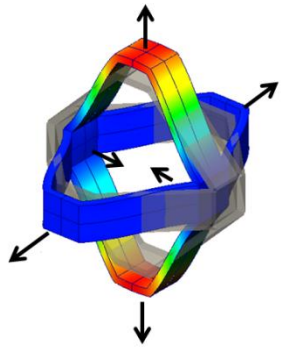

3D cell special configuration